On the Importance of Gradients in the Low-Energy Electron Phase Space Density for Relativistic Electron Acceleration

Hayley J. Allison[1,2] , **Richard B. Horne[1]** , **Sarah A. Glauert[1]** , and **Giulio Del Zanna[2]**

[1]British Antarctic Survey, Natural Environment Research Council, Cambridge, UK, [2]Department of Applied Mathematics and Theoretical Physics, University of Cambridge, Cambridge, UK

Abstract Observations of the electron radiation belts have shown links between increases in the low-energy seed population and enhancements in the >1-MeV flux. During active times, low-energy electrons are introduced to the radiation belt region before being accelerated to higher energies via a range of mechanisms. The impact of variations in the seed population on the 1-MeV flux level were explored using the British Antarctic Survey Radiation Belt Model. We find that, for a period from the 21 April to 9 May 2013, the increase in the low-energy electron flux was vital to recreate the observed 1-MeV flux enhancement on the 1 May but was less important for the 1-MeV enhancement on the 27 April 2013. To better understand the relationships between the different energy populations, a series of idealized experiments with the 2-D British Antarctic Survey Radiation Belt Model were performed, which highlight a careful balance between losses and acceleration from chorus waves. Seed population enhancements alter this balance by increasing the phase space density gradient, and consequently, the rate of energy diffusion, allowing acceleration to surpass loss. Additionally, we demonstrate that even with the same chorus diffusion coefficients and the same low-energy boundary condition, the flux of ~500-keV to 1-MeV electrons increased when starting with a hard spectrum but decreased for a soft initial spectrum. This suggests that initial energy gradients in the phase space density were important to determine whether >500-keV electrons were enhanced due to chorus wave acceleration.

1. Introduction

Whistler mode chorus waves are an important acceleration and loss mechanism in the Earth's electron radiation belts (e.g., Bortnik & Thorne, 2007; Lam et al., 2010; Horne, Thorne, Glauert, et al., 2005; Horne, Thorne, Shprits, et al., 2005; Horne & Thorne, 1998; Summers et al., 1998; Thorne et al., 2005). Recent work considering Van Allen Probes data has highlighted the interplay between the source electrons (1 to tens of kiloelectron volts), responsible for chorus wave generation, and seed electrons (30 to hundreds of kiloelectron volts), in the acceleration of relativistic populations (Jaynes et al., 2015). Substorm particle injections can supply both source and seed electrons to the inner magnetosphere, generating chorus waves and providing an increased low-energy population that can then be accelerated to higher energies (Boyd et al., 2014; DeForest & McIlwain, 1971; Ganushkina et al., 2013; Obara et al., 2000; Omura et al., 2008; Sergeev et al., 1998; Tang et al., 2016; Tsurutani & Smith, 1974; Zhang et al., 2009).

Further observational studies have linked increases in the seed population to those in the core population (>1 MeV). Boyd et al. (2016) demonstrated strong correlations between rises in the seed population and enhancements in the >1-MeV electron flux, with a 10- to 15-hr time delay, highlighting important dependencies between populations of different energies in the radiation belt region. Additionally, correlations between >1-MeV electrons and lower-energy flux values have also been shown using measurements taken at geostationary orbit (Li et al., 2005; Turner & Li, 2008).

A survey of geomagnetically disturbed periods during the Combined Release and Radiation Effects Satellite mission found that the most significant relativistic electron flux enhancements were associated with enhanced seed electron flux and enhanced lower-band chorus wave power (Meredith et al., 2003). Foster et al. (2013) presented Van Allen Probes observations from the March 2013 event and concluded that an increase in the 100-keV flux and chorus wave activity led to prompt energization of highly relativistic electrons outside the plasmapause. Boyd et al. (2014) agreed with this observation, following analysis of observed

phase space density (PSD) profiles from the same event. Using data from both Akebono and the National Oceanic and Atmospheric Administration satellites to study a geomagnetic storm in November 1993, Obara et al. (2000) showed that the enhanced 30- to 100-keV electron flux at $L \sim 4$ seeded the subsequent increase in the >1-MeV electrons.

Observations from a number of satellite missions have therefore strongly suggested that enhancements in the seed population are an important consideration for energization of >1-MeV electrons. However, for electrons with energies less than ~300 keV, interactions with chorus waves result in a competition between acceleration and loss, while above ~300 keV, electrons are accelerated faster than they are lost from the system (Horne, Thorne, Glauert, et al., 2005). As the seed population is thought to primarily cover the energy range ~30 to ~300 keV, this suggests a delicate interplay between both acceleration and loss from chorus waves. As such, changes in the level of the seed population may notably affect the enhancement of >1-MeV populations.

In 3-D radiation belt models, seed population changes are included via the low-energy boundary (LEB) condition. Glauert et al. (2014a) demonstrated that an enhancement of 3-MeV electrons could be achieved by local acceleration of the ~150-keV flux on the LEB. Exploring how changes in the LEB condition affects the flux level at >1 MeV provides an excellent test bed to explore links between the seed population and the core (>1 MeV) population. Despite this, use of numerical models to explore the effect of changes in the seed population has thus far been fairly limited and have provided conflicting results. Using the VERB 3-D model, Subbotin, Shprits, Gkioulidou, et al. (2011) found that the 1-MeV flux was relatively insensitive to the flux at the lowest value of the first adiabatic invariant, μ. However, conversely, Tu et al. (2014) obtained model results that were much closer to observations for the October 2012 "double-dip" storm when a realistic seed population was used for the LEB condition of DREAM 3-D, and event-specific diffusion coefficients were employed.

In this paper, we investigate the effect of changes in the seed population on the 1-MeV electron flux using the British Antarctic Survey Radiation Belt Model (BAS-RBM; Glauert et al., 2014b). In section 3, we compare model results using a LEB condition determined from Van Allen Probe observations to those using time-constant flux values. The results of varying the energies of the LEB are explored in section 4. We then further examine the impact of the seed population in idealized theoretical studies using the 2-D version of the BAS-RBM in sections 5 and 6.

2. BAS Radiation Belt Model

The BAS-RBM is a 3-D diffusion model, based on a simplified version of the Fokker-Planck equation (Schulz & Lanzerotti, 1974), that calculates the evolution of the phase-averaged PSD, $f(p, r, t)$. In the BAS-RBM the diffusion equation has been transformed to equatorial pitch angle, α, energy, E, and L^* coordinates, assuming a dipole magnetic field

$$
\begin{aligned}
\frac{\partial f}{\partial t} =\ & \frac{1}{T(\alpha)\sin(2\alpha)} \left.\frac{\partial}{\partial \alpha}\right|_{E,L^*} \left(T(\alpha)\sin(2\alpha)D_{\alpha\alpha} \left.\frac{\partial f}{\partial \alpha}\right|_{E,L^*} \right) + \\
& \frac{1}{A(E)} \left.\frac{\partial}{\partial E}\right|_{\alpha,L^*} \left(A(E)D_{EE} \left.\frac{\partial f}{\partial E}\right|_{\alpha,L^*} \right) + \\
& L^{*2} \left.\frac{\partial}{\partial L^*}\right|_{\mu,J} \left(\frac{D_{L^*L^*}}{L^{*2}} \left.\frac{\partial f}{\partial L^*}\right|_{\mu,J} \right) - \\
& \frac{f}{\tau_C} - \frac{f}{\tau_M}
\end{aligned}
\tag{1}
$$

where some cross derivatives have been neglected ($D_{E\alpha}$, D_{EL^*}, and $D_{\alpha L^*}$). The function $A(E)$ is given by

$$
A(E) = (E + E_0)(E(E + 2E_0))^{1/2}
\tag{2}
$$

and Roederer's L^* parameter (Roederer, 1970) is defined as

$$
L^* = \frac{2\pi M}{\Phi R_E}.
\tag{3}
$$

E_0 denotes the electron rest mass energy, μ the first adiabatic invariant, J the second adiabatic invariant, and in a dipole field $T(\alpha) = (1.3802 - 0.3198(\sin \alpha + \sin^{1/2} \alpha))$. The L^* parameter is a form of the third adiabatic

invariant, Φ, and in equation 3, M and R_E are respectively the magnetic moment of the Earth's dipole field and the Earth's radius. The timescale for losses to the atmosphere, τ_C, is a quarter of the bounce time inside the loss cone and infinite outside. The drift and bounce-averaged pitch angle and energy diffusion coefficients (D_{EE} and $D_{\alpha\alpha}$) were calculated with the Pitch Angle Diffusion of Ions and Electrons code (Glauert & Horne, 2005) using statistical wave models for whistler mode chorus (Horne et al., 2013), electromagnetic ion cyclotron waves (Kersten et al., 2014), and hiss waves (Meredith et al., 2018). Chorus waves are mainly observed outside the plasmasphere and hiss inside. To account for this, an activity-dependent plasmapause model has been built into the drift and bounce-averaged diffusion coefficients, by considering wave and density observations from the data sets used to construct the statistical wave models (Horne et al., 2013; Meredith et al., 2018). The radial diffusion coefficient, $D_{L^*L^*}$, is taken to be the Kp-dependent magnetic component given by Brautigam and Albert (2000; defined for Kp values between 1 and 6). The magnetopause location is taken from the Shue et al. (1998) model, from which, the last closed drift shell is estimated (Glauert et al., 2014a). The magnetopause loss timescale, τ_M, is set so that the flux is reduced by 3 orders of magnitude in one drift period outside the last closed drift shell. See Glauert et al. (2014b) for further information on the BAS-RBM.

Equation (1) is solved for L^* values $L^*_{\min} \leq L^* \leq L^*_{\max}$, equatorial pitch angles $0° \leq \alpha \leq 90°$, and a range of energies that depend on L^*. As radial diffusion acts at constant first and second adiabatic invariant, the high- and low-energy boundaries follow lines of constant μ and J, defined by selecting the minimum and maximum energies ($E_{\min}$ and $E_{\max}$) at $L^*_{\max}$.

Boundary conditions on six surfaces are required to define the calculation domain, at each of the minimum and maximum values of L^*, α, and energy. Three of these boundary conditions are the same as those used by Glauert et al. (2014b). At $\alpha = 0°$ and $\alpha = 90°$ the change in the phase-averaged PSD with respect to α is set to 0 (i.e., $\frac{\partial f}{\partial \alpha} = 0$). For the $E_{\max}$ boundary, $f = 0$ at the $E_{\max} - \alpha$ surface. The remaining three boundary conditions (f at $L^*_{\min}$, $L^*_{\max}$, and $E_{\min}$) are supplied by data. For the present study, the inner boundary, $L^*_{\min}$, is set at $L^* = 2.5$ and the outer boundary, $L*_{\max}$, at $L^* = 5.5$. Van Allen Probes data from both the Magnetic Electron Ion Spectrometer (MagEIS; Blake et al., 2013) and Relativistic Electron Proton Telescope (REPT; Baker et al., 2013) instruments have been used to formulate $f(\alpha, E, L^*)$ at the $L^*_{\min}$ and $L*_{\max}$ boundary. The final boundary of the BAS-RBM is the $E_{\min}$ boundary, which is discussed at length in the following section.

3. Modeling the 21 April to 9 May 2013 Period

We consider the period from the 21 April to the 9 May 2013. Figures 1a–1e shows the background corrected MagEIS flux from Van Allen Probes A and B. All data presented are from the 90° local pitch angle bin. Additionally, the solar wind speed and z component of the interplanetary magnetic field (B_z) are shown in panel f. The L^* values for the MagEIS measurements in this paper have been calculated using the International Geomagnetic Reference Field (IGRF) and T89 field models (Thébault et al., 2015; Tsyganenko, 1989).

This date range includes two 1-MeV flux enhancement events, separated by a small dropout. The first 1-MeV enhancement period commences late on the 24 April following a dropout, which diminished the preexisting 1-MeV population. This enhancement includes a second stage, relating to a southward turning of B_z early on the 26 April that supplied additional low-energy electrons to the radiation belts (Figures 1a and 1b). After a further dropout on 1 May, a second enhancement of the 1-MeV flux was observed. The second enhancement relates to a longer period of southward B_z and an increased low-energy electron population (Figures 1a–1c) that penetrates further into the radiation belt region. The 1-MeV flux is now more than an order of magnitude higher than the pre-event levels, with both MagEIS instruments recording a 1-MeV electron flux in excess of $10^3 \cdot \mathrm{cm}^{-2} \cdot \mathrm{s}^{-1} \cdot \mathrm{sr}^{-1} \cdot \mathrm{keV}^{-1}$ for much of the outer radiation belt region.

To run the BAS-RBM for the period shown in Figure 1, we formulate a LEB condition from MagEIS observations. The minimum energy for the calculation was selected as ~161 keV at $L^* = 5.5$ ($\mu = 100$ MeV/G for a 90° particle in a dipole magnetic field). Throughout the rest of the paper, the μ value for a 90° particle corresponding to the minimum energy chosen at $L*_{\max}$ will be denoted by $\mu_{\min}$. Two different approaches were taken for calculating the LEB condition. The first involved binning the MagEIS flux into $0.1 L^*$ bins, interpolating the flux to the energy of the LEB, then time averaging over the period (taking the geometric mean). This provided a constant LEB condition, without seed population enhancements, and is shown in Figure 2a.
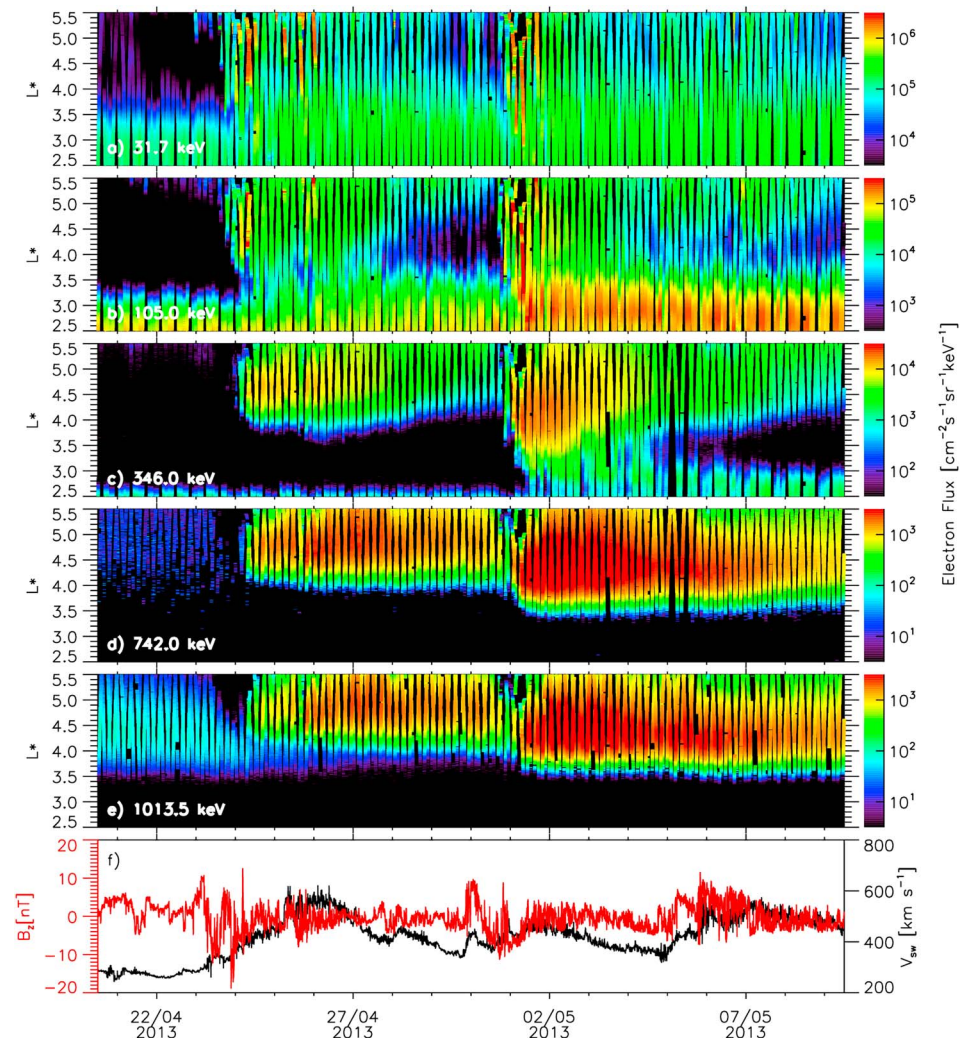
Figure 1. Local perpendicular electron flux from the 31.7-, 105.0-, 346.0-, 742.0-, and 1013.5-keV channels of the Magnetic Electron Ion Spectrometer on board Van Allen Probes A and B (panels a–e) for the period from the 21 April to 9 May 2013. Solar wind speed (black line) and the z component of the interplanetary magnetic field (red line) are shown in panel f.

Second, we used the MagEIS data to formulate a time-dependent LEB condition at the same energies. In this instance, as well as binning the data by $0.1L^*$, the flux was binned into 4.5-hr intervals. The resulting time-varying LEB flux is shown in Figure 2b. Time variations of the electron flux on the LEB spanned more than 2 orders of magnitude, shown by the red line in Figure 2c for $L^* = 4.5$. At the start of the period some of the MagEIS energy channels had missing data as the flux was below the background level. During this time we set the flux to 50 cm^{-2}·s^{-1}·sr^{-1}·keV^{-1} as a value was required for the boundary conditions.

The simulated flux at 1013.5 keV, for 90° pitch angle, resulting from using the constant LEB condition in the BAS-RBM, is shown in Figure 3b. The MagEIS observed flux at this energy is also given in Figure 3a for a local pitch angle of 90° (previously shown in Figure 1e). Both the first and second enhancements of the 1-MeV model flux are lower than observations (Figure 3c). Following the second enhancement event, near $L^* = 4$–5, the 1-MeV population was lower than data by up to a factor of 10. Both enhancements relate to small magnetic storms (Figure 3g), and the AE and Kp indices are given for reference (Figure 3e).

The BAS-RBM was also run using the time-varying LEB condition (Figure 2b), and the resulting electron flux at 1,013.5 keV, 90° pitch angle, is shown in Figure 3d. All the other boundary conditions and the diffusion coefficients were identical to the simulation shown in Figure 3b. Figure 3d reveals that the 1-MeV flux was larger when the time-varying LEB condition was employed, particularly during the second enhancement.
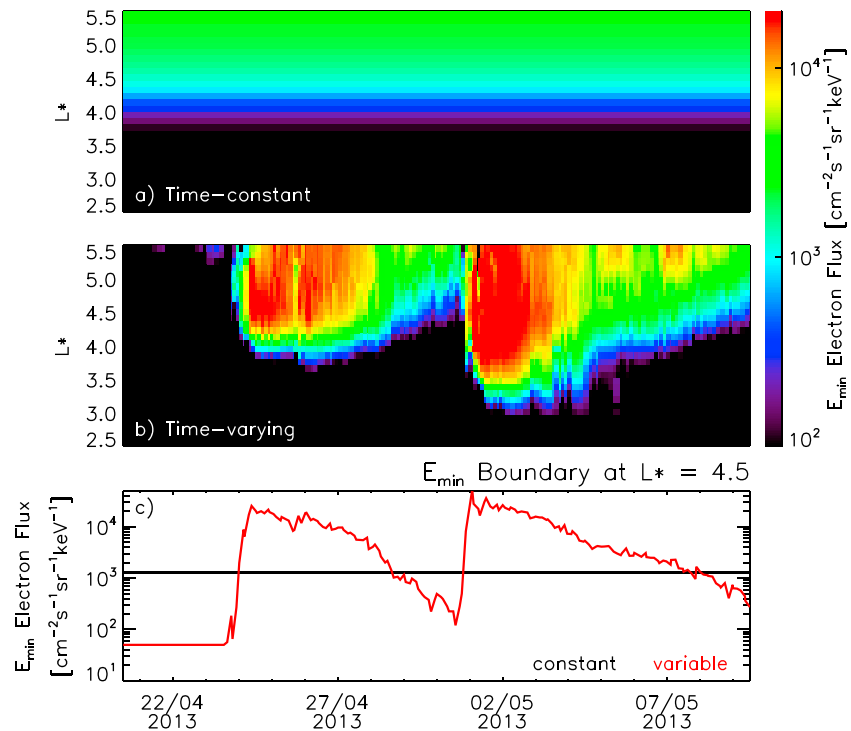
Figure 2. The electron flux along the low-energy boundary (μ_{min} = 100 MeV/G) of the British Antarctic Survey Radiation Belt Model using time-averaged Magnetic Electron Ion Spectrometer data to supply a constant flux profile (panel a) and retaining the temporal information in 4.5-hr intervals (panel b). The electron flux at $L^* = 4.5$ through the constant (black line) and time-varying (red line) low-energy boundary conditions are shown in panel c.

The ratio between the model output and the MagEIS observations (Figure 3e) demonstrates that this second enhancement is now closer to observations for $L^* > 4$ than in the previous model run. The region where the ratio is approximately 1 (white) varies from $L^* = 4.5$ to $L^* = 3.5$ during the period and, following the second enhancement, generally lies at a higher L^* than the simulation with a constant LEB flux.

The results presented in Figure 3 demonstrate that, during the second enhancement event, the rise in the low-energy seed population increased the level of the 1-MeV flux. Chorus wave activity varies throughout the simulation. Increases in the seed population tend to coincide with periods of enhanced AE, and as the chorus diffusion matrix was driven by AE, enhanced chorus diffusion (Horne et al., 2013). The time-varying LEB condition showed similar decay rates for both of the enhancements, and in each instance differed from the constant boundary flux by more than an order of magnitude (Figures 2a and 2b). However, there was a much greater difference between the model results for the second ∼1-MeV enhancement event (1 May) than the first (24 April).

4. Varying the Energy of the LEB

Some radiation belt models use time-invariant LEB conditions (Subbotin, Shprits, Ni, et al., 2011, 2010; Varotsou et al., 2008). These models set the energies of LEB to low values (around 10 keV) where, during active times, the electrons are likely to be on open drift paths due to an enhanced convection electric field (Li et al., 2010; Thorne et al., 2007; Zhang et al., 2015). The assumption is then made that the number of electrons supplied by enhanced convection and those lost on open drift paths and by precipitation ultimately balance and so the level of the flux at these energies remains relatively constant (Subbotin, Shprits, Ni, et al., 2011).

When the LEB is around 10 keV the flux ≳10 keV is determined by diffusion from the LEB and outer boundary condition. However, data show that electrons can be injected into the radiation belt region over a range of energies by electric fields (Dai et al., 2015). Placing the LEB at a higher energy better includes electrons that are from a nondiffusive origin. Additionally, seed population electrons are largely influenced by the convection electric field and the electron flux at these energies is magnetic local time (MLT) dependent during
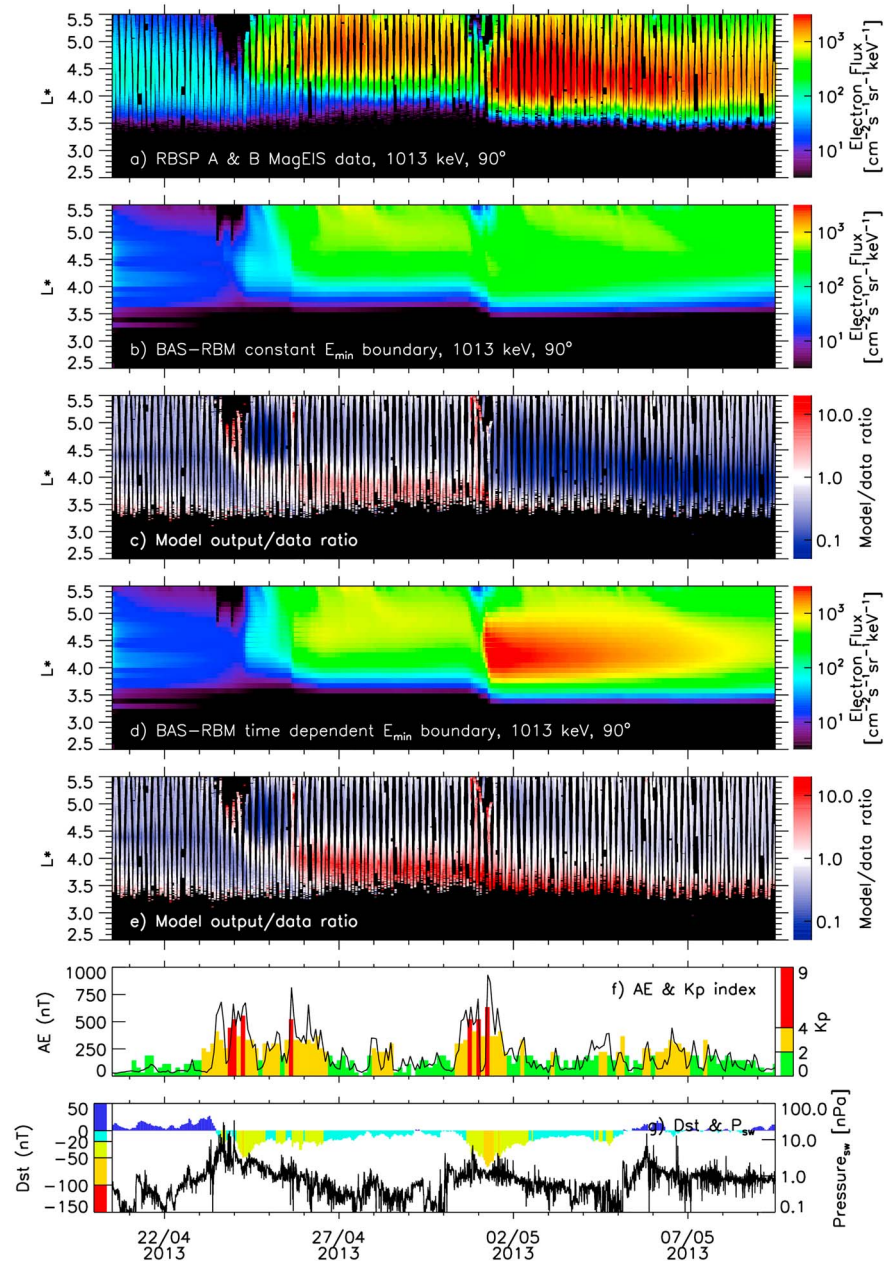
Figure 3. Van Allen Probes A and B Magnetic Electron Ion Spectrometer, 90° local pitch angle, 1,013-keV electron flux observations (panel a). The 1,013-keV, 90° pitch angle flux outputted by the BAS-RBM having used the time-invariant low-energy boundary condition (panel b). Ratio between the model output shown in panel b and the Van Allen Probes observations (panel c). The 1,013 keV, 90° pitch angle flux from the model using the time-varying low-energy boundary condition (panel d). Ratio between the model output shown in panel d and the Van Allen Probes observations (panel e). The AE and Kp indices for the period (panel f). The Dst and solar wind pressure for the period (panel g). RBSP = Radiation Belt Storm Probes; MagEIS = Magnetic Electron Ion Spectrometer; BAS-RBM = British Antarctic Survey Radiation Belt Model.

active times (Allison et al., 2017). As 3-D radiation belt models do not include the MLT dimension, working under a drift-averaged assumption, large MLT asymmetries may introduce errors into the calculation. To avoid MLT variations, some radiation belt models set the LEB at higher energies, away from the convective energy range (Albert et al., 2009; Glauert et al., 2018, 2014a, 2014b).

To investigate the effect of the location of the LEB, we reduce the energies of the LEB condition, setting μ_{min} = 30 MeV/G, and also explore the effect of moving the boundary up in energy, using μ_{min} = 200 MeV/G. In a
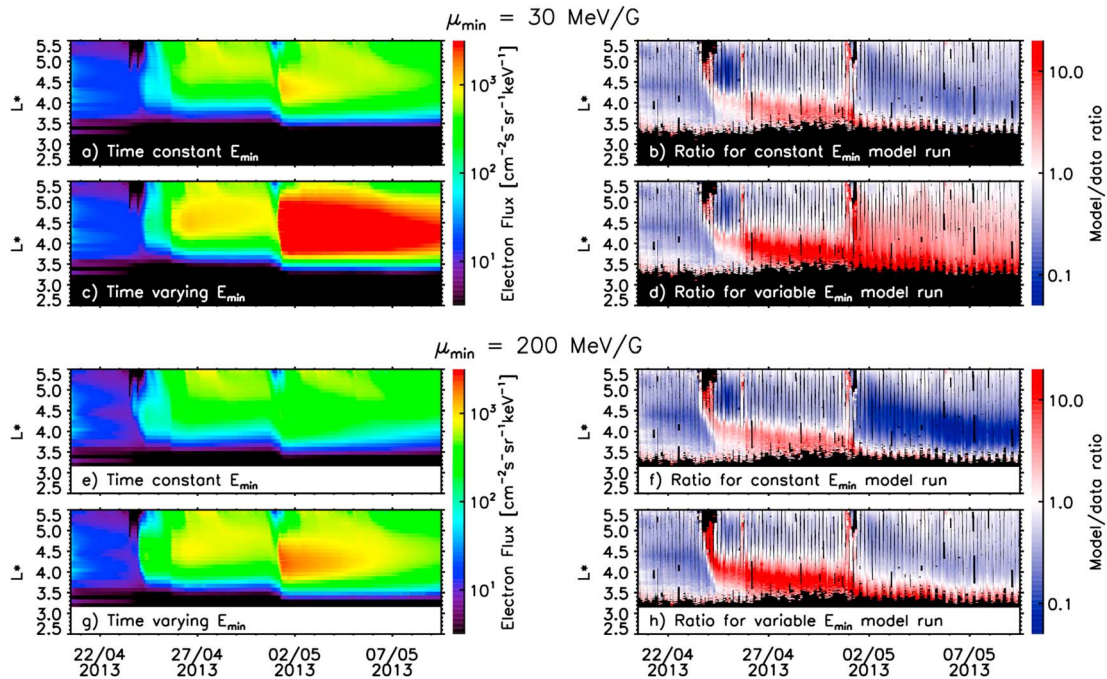
Figure 4. Electron flux from the British Antarctic Survey Radiation Belt Model at 1,013 keV, 90° pitch angle, for time-constant low-energy boundary condition at energies given by μ_{min} = 30 MeV/G (a) and by μ_{min} = 200 MeV/G (e), and for a time-varying low-energy boundary condition at energies given by μ_{min} = 30 MeV/G (c) and by μ_{min} = 200 MeV/G (g). The ratios between the model outputs and the Magnetic Electron Ion Spectrometer observations are shown on the right-hand side for each of the four model runs presented.

dipole field, μ_{min} = 30 MeV/G corresponds to ~53 keV at L^* = 5.5, while μ_{min} = 200 MeV/G, corresponds to ~291 keV. For each value of μ_{min} we calculate both a constant and time-varying LEB condition from MagEIS observations in the manner discussed in section 3.

Figure 4 shows the result of using lower (panels a–d) and higher energies (panels e–h) for the LEB. When using a constant LEB condition, a higher flux at 1 MeV was achieved for μ_{min} = 30 MeV/G (Figure 4a) than for μ_{min} = 100 MeV/G (Figure 3b). Comparing Figure 4c with Figure 3d indicates that the flux was also higher for the μ_{min} = 30 MeV/G time-varying LEB condition. The second 1-MeV flux enhancement, occurring on the 1 May 2013, was nearly a factor of 10 higher than the MagEIS data for 3.5 < L^* < 5 when the μ_{min} = 30 MeV/G time-varying LEB condition was used (Figure 4d).

Conversely, when μ_{min} = 200 MeV/G, the 1-MeV flux was lower than the observations (Figures 4f and 4h) for L^* > 4.5 during the first and second enhancements. Thus, the results indicate that raising the energies of the LEB condition reduced the 1-MeV flux, contrary to what one might expect.

To see how the model results compare to the observed electron spectrum, Figure 5 shows the flux-energy distributions at L^* = 4.5 for selected times, from Van Allen Probe A measurements (panel a) and from the BAS-RBM using constant (panels b, d, and f) and time-varying (panels c, e, and g) LEB conditions. Measurements from the MagEIS instrument are shown as plus symbols, while REPT observations are indicated by diamonds. A slight discontinuity between the MagEIS and REPT observations can be observed, which we have not attempted to resolve, instead choosing to concentrate on the ~1-MeV flux from MagEIS. Vertical dashed lines mark the 1-MeV location for reference.

The model results from the constant LEB condition (Figures 5b, 5d, and 5f) tend to be lower than observations across a broad energy range, which ultimately affected 1-MeV enhancements. However, we note that there was better agreement when the low-energy values were set by smaller μ_{min} (Figure 5b). For some of the selected times, a minimum can be seen near ~200 keV in both the model flux and the Van Allen Probe A measurements. This is due mainly to loss by precipitation in this energy range.

Generally, observed flux levels were best reproduced when the time-varying LEB conditions were used (Figures 5c, 5e, and 5g). As data are used to set the variable LEB condition, the model flux in Figures 5c, 5e,
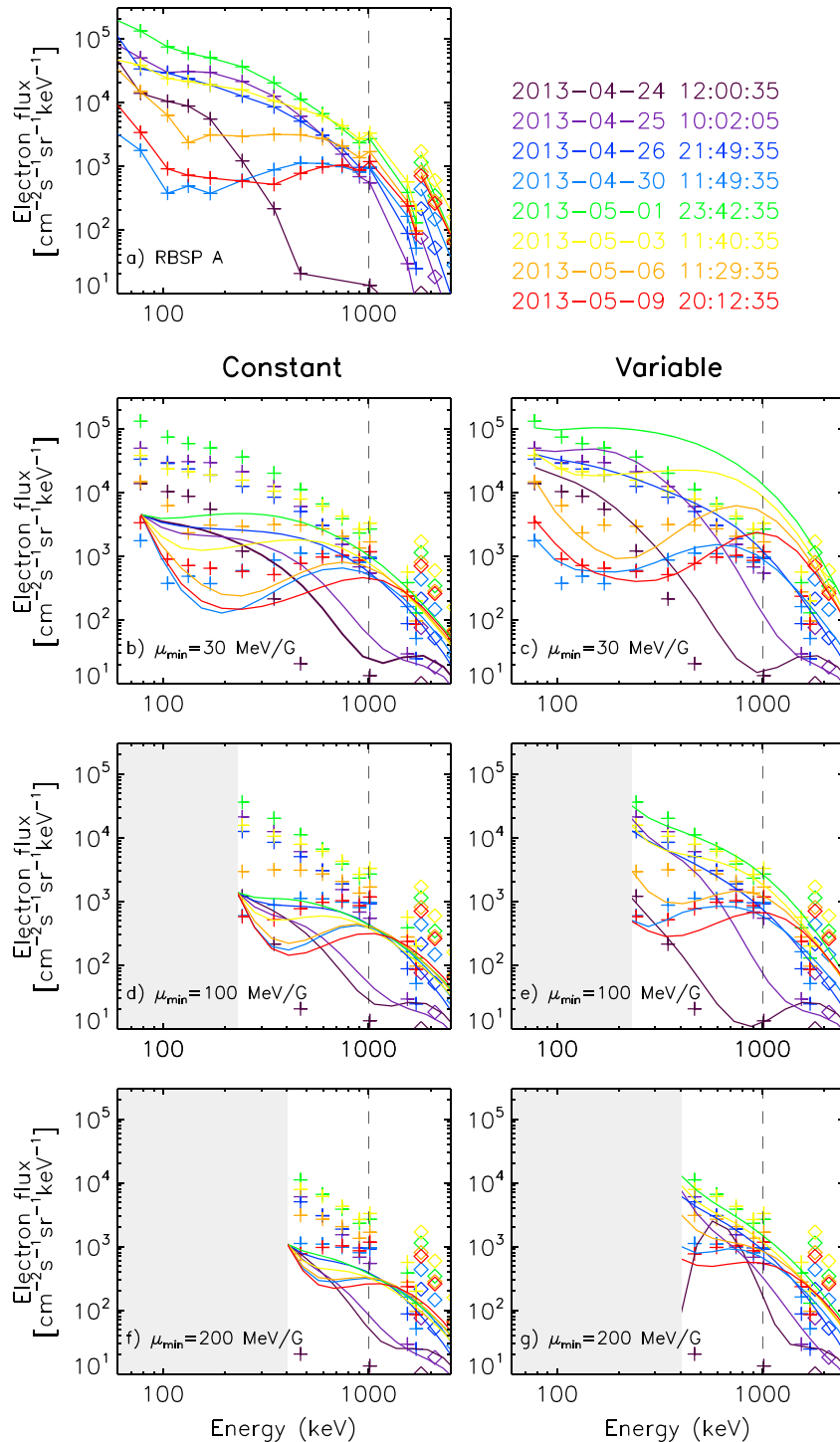
Figure 5. Flux-energy distributions from selected times during the 21 April to 9 May 2013 period at $L^* = 4.5$. (a) The Magnetic Electron Ion Spectrometer (plus symbols) and Relativistic Electron Proton Telescope (diamonds) observations from Van Allen Probe A. These symbols have been added for comparison on all of the panels shown. Additionally, for reference, a vertical dashed line marks 1 MeV. The colored lines in panel (b) show the British Antarctic Survey Radiation Belt Model output from the time-constant low-energy boundary, $\mu_{min} = 30$ MeV/G run and, panel (c), the time-varying low-energy boundary at the same minimum energies. Panels (d) and (e), respectively, show the model outputs for the time-constant and time-varying low-energy boundary conditions at energies given by $\mu_{min} = 100$ MeV/G. Panels (f) and (g) show the model outputs for the time-constant and time-varying low-energy boundary conditions at energies given by $\mu_{min} = 200$ MeV/G. RBSP = Radiation Belt Storm Probes.

and 5g agrees well with observations at energies close to the respective lowest energy, which varies between the three model runs. Using the $\mu_{\min} = 30$ MeV/G time-varying LEB condition (panel c) tended to result in a higher flux during active periods than the MagEIS observations, particularly for energies >400 keV. A peak in the electron flux arises at 24 April 2013 12:00:35 for the $\mu_{\min} = 200$ MeV/G model run shown in Figure 5g (black curve), resulting from a decrease in the variable LEB flux. This spectral form was not reflected by the Van Allen Probe A observations and is discussed further in section 7.

With the exception of periods where "s-shaped" flux-energy distributions are observed (Reeves et al., 2016; Ripoll et al., 2016), the electron flux in the radiation belts generally falls with increasing energy (Cayton et al., 1989). As a result, when the LEB is moved down in energy, the PSD on the boundary will increase. This will raise the maximum PSD that can be achieved by diffusion to higher energies and may be a reason for the higher flux at 1 MeV seen in Figures 4 and 5 when lower values of $\mu_{\min}$ were employed. Another reason is that the 3-D BAS-RBM does not include convection terms and therefore does not include convective loss to the magnetopause. This missing loss process will be most important for the lowest energies that are only included in the simulations with $\mu_{\min} = 30$ MeV/G. In Figure 5c the flux was higher than the data at 1 May 2013 23:42:35, during the second enhancement (green line), for energies $\gtrsim$90 keV. Convective loss would likely reduce the flux at the lowest energies shown here, lowering the available seed population and preventing their acceleration to higher energies. Additionally, the model may underestimate the precipitation during this active period. It is likely that a combination of the above reasons resulted in the model flux exceeding observations for the second 1-MeV enhancement when the $\mu_{\min} = 30$ MeV/G time-varying LEB condition was used.

Another important factor is the efficiency of chorus diffusion for different electron energies. Figure 5 shows more temporal variability in the flux at all energies, including 1 MeV, for lower values of $\mu_{\min}$. Short lived flux enhancements that occur at ~100 keV (see Figure 1b) may be rapidly accelerated by chorus waves, raising the flux at 1 MeV.

5. Size of the Seed Population Enhancement

To understand the effects of chorus waves on the seed population in more detail, we use the 2-D BAS-RBM, neglecting radial diffusion (Horne et al., 2018). We performed an idealized study at $L^* = 4.5$. For the initial condition, the electron PSD was set to a constant value at all energies and pitch angles, except at the LEB, where PSD was set to a value a 100 times higher. Thus, the only initial energy gradient in the calculation was from the LEB condition and all subsequent PSD enhancements in the model originate from diffusing electrons from the LEB. Figure 6a shows the initial PSD profile, with the lowest energy in the calculation set to 10 keV. The chorus diffusion coefficients were held constant for the duration of the simulation, set using AE = 500 nT (Horne et al., 2013) to represent active conditions, and the resulting PSD profile after 24 hr is shown in Figure 6b.

The 10-keV electrons have been accelerated up to ~200 keV by the chorus waves. For the energy range from ~200 to ~900 keV, the PSD has decreased from the initial levels, forming a gap between the <200- and >900-keV energies. Above ~900 keV there has been little-to-no change from the initial condition. Therefore, Figure 6b shows that the 10-keV electrons from the LEB condition were not accelerated up to >1-MeV energies after a day of continuous chorus wave activity.

The same model setup described above was run for a 30-day period, and the results are shown in Figure 6c. Very little difference was observed between the PSD profile after 20 days (not shown) and after 30 days, implying that we are approaching a steady state solution. The PSD gap between ~200 and ~900 keV has persisted even after 30 days, and the 10-keV electrons from the LEB condition were still not accelerated up to >1 MeV, even after a month of continuous chorus wave activity. Either the rate of loss from chorus waves in the 200- to 900-keV energy range was faster than the rate of acceleration, preventing electrons from reaching >900-keV energies, or chorus diffusion was not effective up to 1 MeV for the selected activity. The chorus diffusion coefficients were increased to correspond to AE = 900 nT and the model run again for 30 days (Figure 6d). Even with larger chorus diffusion coefficients, the >1-MeV PSD still did not show an enhancement.

Figure 6e shows the result after running the 2-D BAS-RBM for 30 days with AE = 500 nT where the initial PSD profile was the same as shown in Figure 6a, but the PSD at the LEB was a factor of 100 higher. Now the
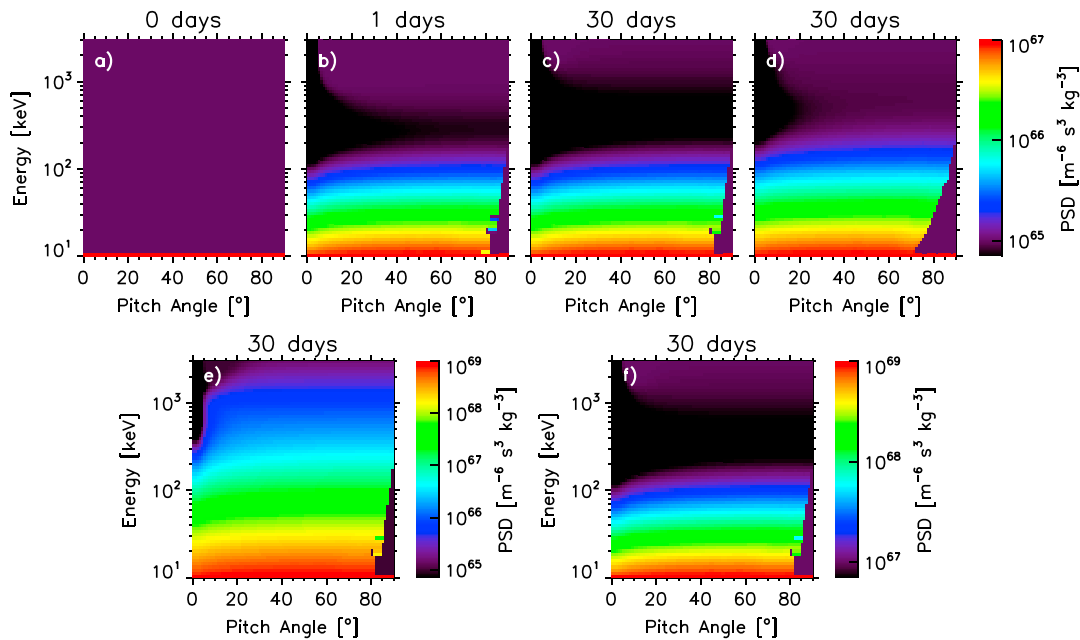
Figure 6. Electron phase space density profiles resulting from idealized experiments with the 2-D British Antarctic Survey Radiation Belt Model. Chorus diffusion rates correspond to (b, c, e, and f) AE = 500 nT, or (d only) AE = 900 nT. Panel (a) shows the shape of the initial PSD distribution used for the model runs in (b)–(d). The resulting PSD is shown after (b) a day and (c) 30 days. Panel (d) shows how the initial PSD in (a) has changed after 30 days, using chorus diffusion coefficients set by a higher activity. In panels (e) and (f), the PSD on the LEB is a factor of 100 higher than in (b)–(d), and the 2-D British Antarctic Survey Radiation Belt Model was run for a 30-day period. The initial PSD, away from the LEB condition, is a factor of 100 higher in (f) than in (e). PSD = phase space density; LEB = low-energy boundary.

10-keV electrons can be accelerated up to >1-MeV energies by chorus waves at $L^* = 4.5$. In Figure 6f, the LEB condition was identical to that used in Figure 6e, but the initial PSD has been raised such that the PSD gradient at the LEB is the same as for Figures 6a–6d. Once the PSD-energy gradient was reduced to previous levels, the >1-MeV electron flux did not show an enhancement after 30 days, even though the PSD level at 10 keV had not changed. It is therefore the gradient in the PSD-energy profile, which is important for the >1-MeV enhancement rather than the level of the PSD on LEB. Increasing the size of PSD-energy gradients ($\frac{\partial f}{\partial E}$ in equation 1) increases the rate of energy diffusion, allowing the energy diffusion to overcome losses and enable an increase in flux all the way up to a few megaelectron volts.

Energy diffusion by chorus waves is not effective at pitch angles near 90° for ≤200-keV electrons (purple area on bottom right of Figures 6b–6f), and as a result, the model gives large pitch angle gradients in this region. For the model results in Figure 6, these large negative pitch angle gradients cause diffusion toward 90°, resulting in PSD enhancements at high pitch angles not seen at lower energies. This is clearest in Figure 6e, where the PSD at 89° is greater than initial levels for energies >200 keV, but for <200 keV, at this pitch angle the PSD has not increased from the initial condition.

Figure 7 considers a wider range of LEB values than Figure 6. Panel (a) shows the ratio at 1 MeV of the PSD after 30 days to the initial PSD, $\alpha = 90°$, $L^* = 4.5$, for different minimum energies. For all model runs, and for the entire 30-day period, we use chorus diffusion coefficients corresponding to AE = 500 nT. A dashed line marks a ratio of 1, separating where the 1 MeV PSD has shown a net decrease after 30 days (<1) from where a net increase was observed (>1). When the LEB was set to 10 keV, an increase in the 1-MeV PSD level was only observed for a boundary PSD of 10^{68} m⁶·s⁻³·kg⁻³ (green curve), otherwise the ratio was less than 1. However, as the energy of the LEB condition was increased, a ratio greater than 1 could be obtained for smaller PSD values. Figure 7a therefore suggests that the 1-MeV population is sensitive to small PSD gradients at a few hundred kiloelectron volts. The electron energies that can be accelerated to 1 MeV are determined by the size of the enhancement and the resulting PSD-energy gradients.

Figure 7b shows the same results as Figure 7a, but at $L^* = 5.5$ instead of $L^* = 4.5$. Very similar trends are observed as seen in Figure 7a; however, for the same energy, moderately smaller PSD enhancements were
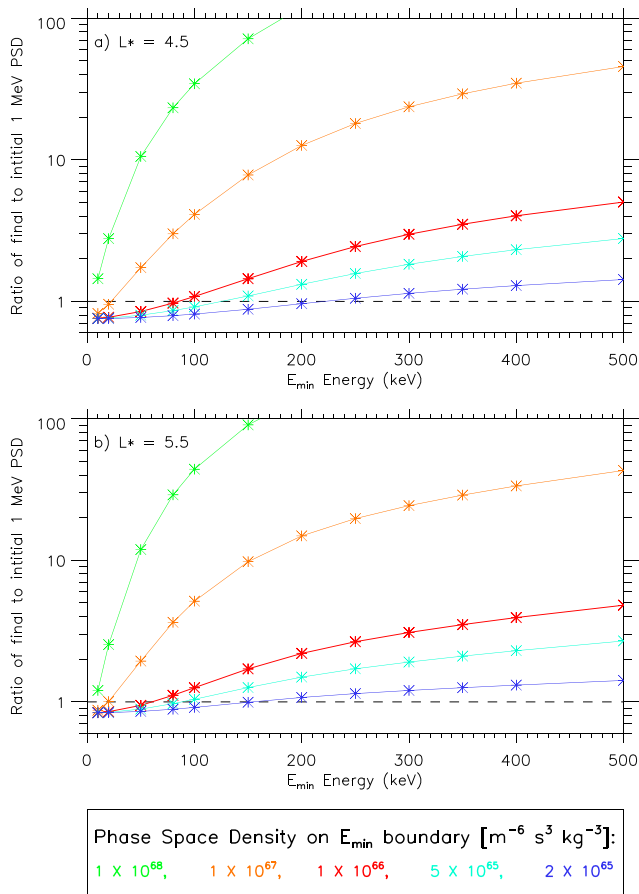
Figure 7. Ratio between the final (after 30 days) and initial phase space density at 1 MeV, 90° pitch angle plotted against the energy at which a phase space density enhancement, of various magnitudes (different colored lines), was supplied. Panel (a) shows the results at $L^* = 4.5$ and panel (b) at $L^* = 5.5$. A dashed line marks the ratio of 1, separating the region where the final 1-MeV phase space density (PSD) was enhanced from where it showed a net decrease. Away from the low-energy boundary, the initial PSD was set to $10^{65} \cdot \mathrm{m}^{-6} \cdot \mathrm{s}^3 \cdot \mathrm{kg}^{-3}$ at all energies and pitch angles.

required to achieve a 1-MeV enhancement. This suggests that, at larger L^*, chorus waves are better able to accelerate lower-energy electrons to >1 MeV energies.

6. Importance of the PSD-Energy Gradients in the Radiation Belt Region

In the simulations presented in section 5, there were initially no gradients in the PSD apart from that at the LEB. To test the importance of initial gradients, Figure 8a presents two 2-D BAS-RBM runs for $L^* = 4.5$, $\alpha = 85°$, each starting with a different PSD distribution, one using a soft spectrum (red dotted line) and the other using a hard spectrum (blue dotted line). In both cases, the same PSD has been used on the LEB and isotropic pitch angle distributions assumed. Only chorus diffusion is included, and again, diffusion coefficients correspond to AE = 500 nT for both runs.

After an hour, the soft spectrum showed an increased PSD for energies ≤350 keV (red dashed line), while, over the same energy range, the PSD of the hard spectrum remained mostly the same as the initial configuration (blue dashed line). Following a day of chorus activity, the soft spectrum (red thick line) showed an increased PSD for <400 keV, but slight PSD decrease at higher energies. In contrast, for the hard spectrum (blue thick line), the PSD has decreased for energies <500 keV but a small increase can be observed in the 500-keV to 1-MeV energy range. Ultimately, both starting PSD distributions evolve to the same steady state, showing the same final form after 30 days (thin red and blue line) and the 1 MeV PSD has decreased from initial levels.

For the hard spectrum, the initial gradients at ~500 keV were such that chorus acceleration to ≥500 keV was faster than the rate of loss. However, as time passed and electrons around 500 keV were lost or accelerated, this gradient shallowed to the point that acceleration to ≥500 keV was no longer faster than the loss rate and the ~500-keV to 1-MeV energy range ultimately experienced a net loss. Due to the initial PSD-energy gradients, the PSD profile evolved differently toward the same steady state form. In this case, whether the ~500-keV to 1-MeV energy range showed an
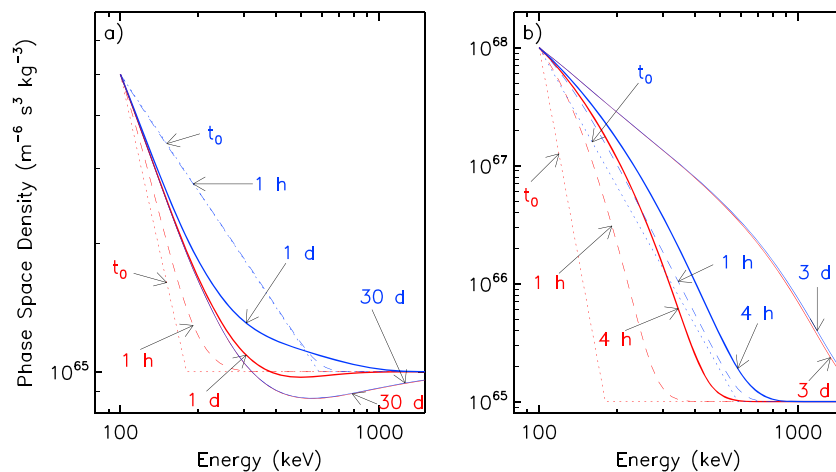
Figure 8. The evolution of different phase space density distributions at $\alpha = 85°$ in the 2-D British Antarctic Survey Radiation Belt Model, one shown in red the other in blue. Two different values for the low-energy boundary phase space density at 100 keV were considered (panels a and b).

enhancement or a decrease depended on the initial PSD energy gradients as well as on the duration of the chorus wave activity.

Figure 8b again shows the evolution of both a hard and soft initial spectrum, but with larger PSD gradients than for Figure 8a (note different scale). The PSD profiles evolved at a faster rate than in Figure 8a for both initial distributions. In this case, the PSD at 1 MeV has increased by a factor of ~7 in 3 days for both the hard and soft spectrum. The larger gradients in PSD cause the two spectra to tend to the same form more rapidly, and show similar PSD values, particularly for energies <800 keV, after 3 days of chorus wave activity.

7. Discussion

Previous work by Reeves et al. (2003) found that only about half of all storms increased the flux of relativistic electrons in the radiations belts. The remaining ~50% either showed no change in the relativistic flux level, or a decrease. Local acceleration by whistler mode chorus waves is thought to be the dominant mechanism for most >1-MeV enhancements in the outer radiation belt region (Boyd et al., 2018). Chorus waves are known to cause both loss and acceleration (Horne, Thorne, Glauert, et al., 2005), and the balance between these two processes is therefore important for determining whether the relativistic electron flux will increase or decrease during a storm. The 2-D BAS-RBM runs shown in Figure 8 demonstrated that, after 1 day, even with the same chorus diffusion coefficients and the same LEB condition, the PSD of the ~500-keV to 1-MeV electrons increased for the soft spectrum, but decreased for the hard spectrum. The preexisting gradients in PSD with energy were important for the rate of energy diffusion, and thus important to determine whether the rate of acceleration by chorus waves was faster than the rate of loss. This suggests that the state of the radiation belts prior to periods of high activity is an important factor to determine whether the relativistic flux level will be enhanced or decreased during an event.

In this paper, we have shown a better agreement between the model and data when we include variations in the seed population (e.g., Figure 3). The results agree with Jaynes et al. (2015) who found that increases in both the source and seed populations were essential for >1-MeV flux enhancements, suggesting that a higher source population led to higher chorus wave power. However, Jaynes et al. (2015) drew their conclusions from interpreting observations, whereas in this paper we have used a chorus wave model (Horne et al., 2013) and calculated the effect on the electron flux to show explicitly that the seed population increase was an important component leading to the second 1-MeV enhancement in the 21 April to 9 May 2013 period.

Using time-varying event-specific LEB conditions in the 3-D BAS-RBM allows the PSD on the LEB condition to decrease as well as increase. Considering Figure 5g, the data show low flux over a range of energies at 24 April 2013 12:00:35 following a flux dropout (black symbols). Corresponding to this, the LEB condition was reduced, introducing positive gradients in the energy spectrum (black line). A decrease in the LEB may result in diffusion to lower energies, if chorus waves are present, reducing the PSD in the calculation. However, the agreement between model and data at subsequent times in Figure 5g was better than when using a constant LEB condition (Figure 5f). Additionally, Figures 3 and 4 show that larger 1-MeV flux values were produced when time-varying LEB conditions were used, suggesting that the net effect was to increase the electron flux. It would therefore appear that possible PSD reductions only made a small contribution. This is likely because, generally, the low-energy populations will decrease during quiet times, when diffusion coefficients are lower.

While whistler mode chorus waves have been shown to be a particularly important acceleration mechanism (Bortnik & Thorne, 2007; Horne & Thorne, 1998; Horne, Thorne, Glauert, et al., 2005; Horne, Thorne, Shprits, et al., 2005; Summers et al., 1998; Thorne et al., 2005), other processes, such as radial diffusion, have a considerable impact on the radiation belt region (Shprits & Thorne, 2004; Su et al., 2010). The experiments with the 2-D BAS-RBM presented in sections 5 and 6 were very idealized and provided an investigative tool in order to better understand the energy dynamics in the radiation belts, omitting radial diffusion. In reality, the standard picture is likely more of a three-step process, where the seed populations are enhanced, locally accelerated by chorus waves, and then redistributed by radial diffusion (e.g., Horne, 2007), further increasing the electron energy by inward motion (Boyd et al., 2014; Thorne et al., 2013). As a result, radial diffusion of locally energized electrons to lower L^* values could produce >1 MeV electrons from the seed population enhancement, even if the PSD-energy gradients were not sufficient for local acceleration to >1-MeV energies from chorus waves alone.

Figures 3 and 6 demonstrated that PSD gradients introduced by enhancements in the LEB condition were important to determine whether the 1-MeV population was enhanced by chorus wave activity. We note that diffusion could drive variations in these gradients faster than the LEB condition is updated. By setting the LEB condition from observations, the update rate was limited by the orbital period of the satellite (satellites), in this case the Van Allen Probes. Future work will focus on using a data-driven LEB condition with a higher time resolution, such as those derived from low earth orbit observations (Allison et al., 2018), to better include changing PSD gradients and determine the effect on the model result.

The Van Allen Probes precess slowly in MLT, and therefore for a particular L^*, supply seed population observations localized in MLT. However, during active periods, as the dynamics of the lower-energy populations are so affected by the convection electric field (Califf et al., 2017), the seed population can be highly MLT dependent (Allison et al., 2017), with higher flux in the dawn-sector than the dusk. Therefore, one would expect the PSD gradients at seed population energies to also be higher on the dawn side of the Earth. Chorus waves are mainly observed in the nightside, dawnside, and dayside MLT sectors (Meredith et al., 2012). Therefore, larger PSD gradients are present in regions of chorus wave propagation than otherwise. Up-and-coming 4-D radiation belt models will allow for further exploration of MLT dependent PSD-energy gradients (Shprits et al., 2015).

8. Conclusions

Using both the 3-D and 2-D BAS-RBM, the effect of changes in the seed population has been explored. Two enhancement events between the 21 April to 9 May 2013 period were studied using the 3-D model, including and excluding seed population enhancements and varying the energies of the LEB condition. Using the 2-D BAS-RBM, a number of idealized experiments were performed in order to better understand the effect of chorus waves on the seed population. The main conclusions are as follows:

1. The $\mu_{\min} = 100$ MeV/G time-varying LEB condition resulted in better agreement with Van Allen Probes observations at 1 MeV than using a constant LEB flux. The seed population enhancement was an important component to recreate the level of the 1 MeV following the 1 May 2013.
2. Contrary to expectation, raising the energies of the LEB ($\mu_{\min} = 200$ MeV/G) led to lower flux at 1 MeV and a poorer agreement with data than using $\mu_{min} = 100$ MeV/G. Reducing the energies of the LEB ($\mu_{\min} = 30$ MeV/G) raised the flux at 1 MeV but, during active periods, produced a flux higher than observations across a broad range of energies.
3. Low-energy enhancements change the PSD-energy gradients and can result in faster energy diffusion. Chorus waves cause both acceleration and loss and, at the lowest energies, there is a delicate balance between these two processes. Large enough PSD gradients in energy increase the rate of energy diffusion, and can therefore overcome the rate of loss, allowing electrons to be accelerated to ~1 MeV by chorus waves.
4. Using a constant LEB condition and chorus diffusion coefficients, the PSD tended toward a steady state for either a hard or soft spectrum. However, the evolution was different, and therefore, the initial PSD-energy gradients prior to an event are very important in determining the response of the 1-MeV population.

The results presented in this paper have highlighted the importance of gradients in the PSD with energy, which may differ between the dawn and dusk MLT sectors. For a more realistic analysis of radiation belt variability we should consider the different PSD energy gradients.

References

Albert, J. M., Meredith, N. P., & Horne, R. B. (2009). Three-dimensional diffusion simulation of outer radiation belt electrons during the 9 October 1990 magnetic storm. *Journal of Geophysical Research*, *114*, A09214. https://doi.org/10.1029/2009JA014336

Allison, H. J., Horne, R. B., Glauert, S. A., & Del Zanna, G. (2017). The magnetic local time distribution of energetic electrons in the radiation belt region. *Journal of Geophysical Research: Space Physics*, *122*, 8108–8123. https://doi.org/10.1002/2017JA024084

Allison, H. J., Horne, R. B., Glauert, S. A., & Del Zanna, G. (2018). Determination of the equatorial electron differential flux from observations at low Earth orbit. *Journal of Geophysical Research: Space Physics*, *123*, 9574–9596. https://doi.org/10.1029/2018JA025786

Baker, D. N., Kanekal, S. G., Hoxie, V. C., Batiste, S., Bolton, M., Li, X., et al. (2013). The relativistic electron-proton telescope (REPT) instrument on board the Radiation Belt Storm Probes (RBSP) spacecraft: Characterization of earth's radiation belt high-energy particle populations. *Space Science Reviews*, *179*(1), 337–381. https://doi.org/10.1007/s11214-012-9950-9

Blake, J. B., Carranza, P. A., Claudepierre, S. G., Clemmons, J. H., Crain, W. R., Dotan, Y., et al. (2013). The Magnetic Electron Ion Spectrometer (MagEIS) instruments aboard the Radiation Belt Storm probes (RBSP) spacecraft. *Space Science Reviews*, *179*(1), 383–421. https://doi.org/10.1007/s11214-013-9991-8

Bortnik, J., & Thorne, R. (2007). The dual role of ELF/VLF chorus waves in the acceleration and precipitation of radiation belt electrons. *Journal of Atmospheric and Solar-Terrestrial Physics*, *69*(3), 378–386. https://doi.org/10.1016/j.jastp.2006.05.030, global Aspects of Magnetosphere-Ionosphere Coupling.

Boyd, A. J., Spence, H. E., Claudepierre, S. G., Fennell, J. F., Blake, J. B., Baker, D. N., et al. (2014). Quantifying the radiation belt seed population in the 17 March 2013 electron acceleration event. *Geophysical Research Letters*, *41*, 2275–2281. https://doi.org/10.1002/2014GL059626

Boyd, A. J., Spence, H. E., Huang, C.-L., Reeves, G. D., Baker, D. N., Turner, D. L., et al. (2016). Statistical properties of the radiation belt seed population. *Journal of Geophysical Research: Space Physics*, *121*, 7636–7646. https://doi.org/10.1002/2016JA022652

Boyd, A. J., Turner, D. L., Reeves, G. D., Spence, H. E., Baker, D. N., & Blake, J. B. (2018). What causes radiation belt enhancements: A survey of the Van Allen Probes era. *Geophysical Research Letters*, *45*, 5253–5259. https://doi.org/10.1029/2018GL077699

Brautigam, D. H., & Albert, J. M. (2000). Radial diffusion analysis of outer radiation belt electrons during the October 9, 1990, magnetic storm. *Journal of Geophysical Research*, *105*(A1), 291–309. https://doi.org/10.1029/1999JA900344

Califf, S., Li, X., Zhao, H., Kellerman, A., Sarris, T. E., Jaynes, A., & Malaspina, D. M. (2017). The role of the convection electric field in filling the slot region between the inner and outer radiation belts. *Journal of Geophysical Research: Space Physics*, *122*, 2051–2068. https://doi.org/10.1002/2016JA023657

Cayton, T. E., Belian, R. D., Gary, S. P., Fritz, T. A., & Baker, D. N. (1989). Energetic electron components at geosynchronous orbit. *Geophysical Research Letters*, *16*(2), 147–150. https://doi.org/10.1029/GL016i002p00147

Dai, L., Wang, C., Duan, S., He, Z., Wygant, J. R., Cattell, C. A., et al. (2015). Near-Earth injection of MeV electrons associated with intense dipolarization electric fields: Van Allen Probes observations. *Geophysical Research Letters*, *42*, 6170–6179. https://doi.org/10.1002/2015GL064955

DeForest, S. E., & McIlwain, C. E. (1971). Plasma clouds in the magnetosphere. *Journal of Geophysical Research*, *76*(16), 3587–3611. https://doi.org/10.1029/JA076i016p03587

Foster, J. C., Erickson, P. J., Baker, D. N., Claudepierre, S. G., Kletzing, C. A., Kurth, W., et al. (2013). Prompt energization of relativistic and highly relativistic electrons during a substorm interval: Van Allen Probes observations. *Geophysical Research Letters*, *41*, 20–25. https://doi.org/10.1002/2013GL058438

Ganushkina, N. Y., Liemohn, M. W., Amariutei, O. A., & Pitchford, D. (2013). Low-energy electrons (5-50 keV) in the inner magnetosphere. *Journal of Geophysical Research: Space Physics*, *119*, 246–259. https://doi.org/10.1002/2013JA019304

Glauert, S. A., & Horne, R. B. (2005). Calculation of pitch angle and energy diffusion coefficients with the PADIE code. *Journal of Geophysical Research*, *110*, A04206. https://doi.org/10.1029/2004JA010851

Glauert, S. A., Horne, R. B., & Meredith, N. P. (2014a). Simulating the Earth's radiation belts: Internal acceleration and continuous losses to the magnetopause. *Journal of Geophysical Research: Space Physics*, *119*, 7444–7463. https://doi.org/10.1002/2014JA020092

Glauert, S. A., Horne, R. B., & Meredith, N. P. (2014b). Three-dimensional electron radiation belt simulations using the BAS radiation belt model with new diffusion models for chorus, plasmaspheric hiss, and lightning-generated whistlers. *Journal of Geophysical Research: Space Physics*, *119*, 268–289. https://doi.org/10.1002/2013JA019281

Glauert, S. A., Horne, R. B., & Meredith, N. P. (2018). A 30-year simulation of the outer electron radiation belt. *Space Weather*, *16*, 1498–1522. https://doi.org/10.1029/2018SW001981

Horne, R. B. (2007). Acceleration of killer electrons. *Nature Physics*, *3*, 590–591.

Horne, R. B., Kersten, T., Glauert, S. A., Meredith, N. P., Boscher, D., Sicard-Piet, A., et al. (2013). A new diffusion matrix for whistler mode chorus waves. *Journal of Geophysical Research: Space Physics*, *118*, 6302–6318. https://doi.org/10.1002/jgra.50594

Horne, R. B., Phillips, M. W., Glauert, S. A., Meredith, N. P., Hands, A. D. P., Ryden, K. A., & Li, W. (2018). Realistic worst case for a severe space weather event driven by a fast solar wind stream. *Space Weather*, *16*, 1202–1215. https://doi.org/10.1029/2018SW001948

Horne, R. B., & Thorne, R. M. (1998). Potential waves for relativistic electron scattering and stochastic acceleration during magnetic storms. *Geophysical Research Letters*, *25*(15), 3011–3014. https://doi.org/10.1029/98GL01002

Horne, R. B., Thorne, R. M., Glauert, S. A., Albert, J. M., Meredith, N. P., & Anderson, R. R. (2005). Timescale for radiation belt electron acceleration by whistler mode chorus waves. *Journal of Geophysical Research*, *110*, A03225. https://doi.org/10.1029/2004JA010811

Horne, R. B., Thorne, R. M., Shprits, Y. Y., Meredith, N. P., Glauert, S. A., Smith, A. J., et al. (2005). Wave acceleration of electrons in the Van Allen radiation belts. *Nature*, *437*(7056), 227–230. https://doi.org/10.1038/nature03939

Jaynes, A. N., Baker, D. N., Singer, H. J., Rodriguez, J. V., Loto'aniu, T. M., Ali, A. F., et al. (2015). Source and seed populations for relativistic electrons: Their roles in radiation belt changes. *Journal of Geophysical Research: Space Physics*, *120*, 7240–7254. https://doi.org/10.1002/2015JA021234

Kersten, T., Horne, R. B., Glauert, S. A., Meredith, N. P., Fraser, B. J., & Grew, R. S. (2014). Electron losses from the radiation belts caused by EMIC waves. *Journal of Geophysical Research: Space Physics*, *119*, 8820–8837. https://doi.org/10.1002/2014JA020366

Lam, M. M., Horne, R. B., Meredith, N. P., Glauert, S. A., Moffat-Griffin, T., & Green, J. C. (2010). Origin of energetic electron precipitation >30 keV into the atmosphere. *Journal of Geophysical Research*, *115*, A00F08. https://doi.org/10.1029/2009JA014619

Li, X., Baker, D. N., Temerin, M., Reeves, G., Friedel, R., & Shen, C. (2005). Energetic electrons, 50 keV to 6 MeV, at geosynchronous orbit: Their responses to solar wind variations. *Space Weather*, *3*, 04001. https://doi.org/10.1029/2004SW000105

Li, W., Thorne, R. M., Bortnik, J., Nishimura, Y., Angelopoulos, V., Chen, L., et al. (2010). Global distributions of suprathermal electrons observed on THEMIS and potential mechanisms for access into the plasmasphere. *Journal of Geophysical Research*, *115*, A00J10. https://doi.org/10.1029/2010JA015687

Meredith, N. P., Cain, M., Horne, R. B., Thorne, R. M., Summers, D., & Anderson, R. R. (2003). Evidence for chorus-driven electron acceleration to relativistic energies from a survey of geomagnetically disturbed periods. *Journal of Geophysical Research*, *108*(A6), 1248. https://doi.org/10.1029/2002JA009764

Meredith, N. P., Horne, R. B., Kersten, T., Li, W., Bortnik, J., Sicard, A., & Yearby, K. H. (2018). Global model of plasmaspheric hiss from multiple satellite observations. *Journal of Geophysical Research: Space Physics*, *123*, 4526–4541. https://doi.org/10.1029/2018JA025226

Meredith, N. P., Horne, R. B., Sicard-Piet, A., Boscher, D., Yearby, K. H., Li, W., & Thorne, R. M. (2012). Global model of lower band and upper band chorus from multiple satellite observations. *Journal of Geophysical Research*, *117*, A10225. https://doi.org/10.1029/2012JA017978

Obara, T., Nagatsuma, T., Den, M., Miyoshi, Y., & Morioka, A. (2000). Main-phase creation of "seed" electrons in the outer radiation belt. *Earth, Planets and Space*, *52*(1), 41–47. https://doi.org/10.1186/BF03351612

Omura, Y., Katoh, Y., & Summers, D. (2008). Theory and simulation of the generation of whistler-mode chorus. *Journal of Geophysical Research*, *113*, A04223. https://doi.org/10.1029/2007JA012622

Reeves, G. D., Friedel, R. H. W., Larsen, B. A., Skoug, R. M., Funsten, H. O., Claudepierre, S. G., et al. (2016). Energy-dependent dynamics of keV to MeV electrons in the inner zone, outer zone, and slot regions. *Journal of Geophysical Research: Space Physics*, *121*, 397–412. https://doi.org/10.1002/2015JA021569

Reeves, G. D., McAdams, K. L., Friedel, R. H. W., & O'Brien, T. P. (2003). Acceleration and loss of relativistic electrons during geomagnetic storms. *Geophysical Research Letters*, *30*(10), 1529. https://doi.org/10.1029/2002GL016513

Ripoll, J.-F., Reeves, G. D., Cunningham, G. S., Loridan, V., Denton, M., Santolík, O., et al. (2016). Reproducing the observed energy-dependent structure of Earth's electron radiation belts during storm recovery with an event-specific diffusion model. *Geophysical Research Letters*, *43*, 5616–5625. https://doi.org/10.1002/2016GL068869

Roederer, J. G. (1970). *Dynamics of geomagnetically trapped radiation* (Vol. 2, 1st ed.). Heidelberg, New York: Springer-Verlag Berlin.

Schulz, M., & Lanzerotti, L. J. (1974). *Particle diffusion in the radiation belts*. Berlin, Heidelberg, New York: Springer-Verlag.

Sergeev, V. A., Shukhtina, M. A., Rasinkangas, R., Korth, A., Reeves, G. D., Singer, H. J., et al. (1998). Event study of deep energetic particle injections during substorm. *Journal of Geophysical Research*, *103*(A5), 9217–9234. https://doi.org/10.1029/97JA03686

Shprits, Y. Y., Kellerman, A. C., Drozdov, A. Y., Spence, H. E., Reeves, G. D., & Baker, D. N. (2015). Combined convective and diffusive simulations: VERB-4D comparison with 17 March 2013 Van Allen Probes observations. *Geophysical Research Letters*, *42*, 9600–9608. https://doi.org/10.1002/2015GL065230

Shprits, Y. Y., & Thorne, R. M. (2004). Time dependent radial diffusion modeling of relativistic electrons with realistic loss rates. *Geophysical Research Letters*, *31*, L08805. https://doi.org/10.1029/2004GL019591

Shue, J.-H., Song, P., Russell, C. T., Steinberg, J. T., Chao, J. K., Zastenker, G., et al. (1998). Magnetopause location under extreme solar wind conditions. *Journal of Geophysical Research*, *103*(A8), 17,691–17,700. https://doi.org/10.1029/98JA01103

Su, Z., Xiao, F., Zheng, H., & Wang, S. (2010). STEERB: A three-dimensional code for storm-time evolution of electron radiation belt. *Journal of Geophysical Research*, *115*, A09208. https://doi.org/10.1029/2009JA015210

Subbotin, D. A., Shprits, Y. Y., Gkioulidou, M., Lyons, L. R., Ni, B., Merkin, V. G., et al. (2011). Simulation of the acceleration of relativistic electrons in the inner magnetosphere using RCM-VERB coupled codes. *Journal of Geophysical Research*, *116*, A08211. https://doi.org/10.1029/2010JA016350

Subbotin, D., Shprits, Y., & Ni, B. (2010). Three-dimensional VERB radiation belt simulations including mixed diffusion. *Journal of Geophysical Research*, *115*, A03205. https://doi.org/10.1029/2009JA015070

Subbotin, D. A., Shprits, Y. Y., & Ni, B. (2011). Long-term radiation belt simulation with the VERB 3-D code: Comparison with CRRES observations. *Journal of Geophysical Research*, *116*, A12210. https://doi.org/10.1029/2011JA017019

Summers, D., Thorne, R. M., & Xiao, F. (1998). Relativistic theory of wave-particle resonant diffusion with application to electron acceleration in the magnetosphere. *Journal of Geophysical Research*, *103*(A9), 20,487–20,500. https://doi.org/10.1029/98JA01740

Tang, C. L., Zhang, J.-C., Reeves, G. D., Su, Z. P., Baker, D. N., Spence, H. E., et al. (2016). Prompt enhancement of the Earth's outer radiation belt due to substorm electron injections. *Journal of Geophysical Research: Space Physics*, *121*, 11,826–11,838. https://doi.org/10.1002/2016JA023550

Thébault, E., Finlay, C. C., Beggan, C. D., Alken, P., Aubert, J., Barrois, O., et al. (2015). International geomagnetic reference field: The 12th generation. *Earth, Planets and Space*, *67*(1), 79. https://doi.org/10.1186/s40623-015-0228-9

Thorne, R. M., Li, W., Ni, B., Ma, Q., Bortnik, J., Chen, L., et al. (2013). Rapid local acceleration of relativistic radiation-belt electrons by magnetospheric chorus. *Nature*, *504*, 411–414.

Thorne, R. M., O'Brien, T. P., Shprits, Y. Y., Summers, D., & Horne, R. B. (2005). Timescale for MeV electron microburst loss during geomagnetic storms. *Journal of Geophysical Research*, *110*, A09202. https://doi.org/10.1029/2004JA010882

Thorne, R. M., Shprits, Y. Y., Meredith, N. P., Horne, R. B., Li, W., & Lyons, L. R. (2007). Refilling of the slot region between the inner and outer electron radiation belts during geomagnetic storms. *Journal of Geophysical Research*, *112*, A06203. https://doi.org/10.1029/2006JA012176

Tsurutani, B. T., & Smith, E. J. (1974). Postmidnight chorus: A substorm phenomenon. *Journal of Geophysical Research*, *79*(1), 118–127. https://doi.org/10.1029/JA079i001p00118

Tsyganenko, N. (1989). A magnetospheric magnetic field model with a warped tail current sheet. *Planetary and Space Science*, *37*(1), 5–20. https://doi.org/10.1016/0032-0633(89)90066-4

Tu, W., Cunningham, G. S., Chen, Y., Morley, S. K., Reeves, G. D., Blake, J. B., et al. (2014). Event-specific chorus wave and electron seed population models in dream3d using the Van Allen Probes. *Geophysical Research Letters*, *41*, 1359–1366. https://doi.org/10.1002/2013GL058819

Turner, D. L., & Li, X. (2008). Quantitative forecast of relativistic electron flux at geosynchronous orbit based on low-energy electron flux. *Space Weather*, *6*, 05005. https://doi.org/10.1029/2007SW000354

Varotsou, A., Boscher, D., Bourdarie, S., Horne, R. B., Meredith, N. P., Glauert, S. A., & Friedel, R. H. (2008). Three-dimensional test simulations of the outer radiation belt electron dynamics including electron-chorus resonant interactions. *Journal of Geophysical Research*, *113*, A12212. https://doi.org/10.1029/2007JA012862

Zhang, D., Cao, J. B., Wei, X. H., & Li, L. Y. (2015). New technique to calculate electron Alfvén layer and its application in interpreting geosynchronous access of ps energetic electrons. *Journal of Geophysical Research: Space Physics*, *120*, 1675–1683. https://doi.org/10.1002/2014JA020670

Zhang, J.-C., Wolf, R. A., Spiro, R. W., Erickson, G. M., Sazykin, S., Toffoletto, F. R., & Yang, J. (2009). Rice convection model simulation of the substorm-associated injection of an observed plasma bubble into the inner magnetosphere: 2. Simulation results. *Journal of Geophysical Research*, *114*, A08219. https://doi.org/10.1029/2009JA014131